Nanogap Traps for Passive Bacteria Concentration and Single-Point Confocal Raman Spectroscopy

Jung Y. Han,[†] Michael Yeh, and Don L. DeVoe[*]

Department of Mechanical Engineering, University of Maryland, College Park, MD, USA
[†]Current affiliation: Department of Bionanotechnology, Gachon University, Seongnam-si, South Korea
[*]Corresponding author: ddev@umd.edu

Abstract

A microfluidic device enabling the isolation and concentration of bacteria for analysis by confocal Raman spectroscopy is presented. The glass-on-silicon device employs a tapered chamber surrounded by a 500 nm gap that serves to concentrate cells at the chamber apex during sample perfusion. The sub-micrometer gaps retain bacteria by size exclusion while allowing smaller contaminants to pass unimpeded. Concentrating bacteria within the fixed volume enables the use of single-point confocal Raman detection for the rapid acquisition of spectral signatures for bacteria identification. The technology is evaluated for the analysis of *E. cloacae*, *K. pneumoniae* and *C. diphtheriae*, with automated peak extraction yielding distinct spectral fingerprints for each pathogen at a concentration of 10^3 CFU/mL that compare favorably with spectra obtained from significantly higher concentration reference samples evaluated by conventional confocal Raman analysis. The nanogap technology offers a simple, robust, and passive approach to concentrating bacteria from dilute samples into a well-defined optical detection volume, enabling rapid and sensitive confocal Raman detection for label-free identification of focused cells.

Introduction

The identification of bacteria is an essential task in many microbiological workflows. In addition to the need for determining the causative agents involved in bacterial infections, bacteria identification is important for a broader range of application ranging from epidemiologic studies to food safety and beyond. Bacteria identification is also an important step in the process of screening for antibiotic resistance, which presents a significant and growing public health challenge.[1] The classical approach to identifying bacteria involves the use of cell culture followed by phenotypic characterization based on cell morphology, staining, or various biochemical assays.[2] However, not all organisms can be cultured *in vitro*, and culture-based assays typically require several days to generate actionable results.[3] Because of the long time scale for culture-based bacteria identification, treatment selection often relies on clinical observation alone, resulting in the unnecessary use of broad spectrum drugs and leading directly to the increasing prevalence of antibiotic resistant pathogens.[4] It is widely recognized that new culture-free assays are needed to improve clinical decision-making for bacterial infections.[5] To overcome these limitations, rapid culture-independent molecular assays have emerged as a powerful alternative for bacterial identification, with the most common approach based on multiplexed PCR targeting the high-conserved 16S rRNA gene that presents species-specific regions.[6] While genotypic assays can be significantly faster than culture-based characterization, these test remain cumbersome and expensive, and offer limited agility in adapting to new pathogens.

Raman spectroscopy is an optical imaging technique that has been successfully harnessed to evaluate bacteria from clinical specimens. Raman spectra contain information from the inelastic scattering of light due to the vibrational and rotational states of the target molecules.[7] The technique is a label-free approach that can generate pathogen-specific fingerprints reflecting distinct bacterial phenotypes based on specific molecular attributes.[8] Raman imaging has been widely demonstrated for strain-level bacteria

identification[9–11] and sub-typing,[12,13] and the use of machine learning techniques for automated feature classification have enabled a wide range of bacterial pathogens to be identified from clinical isolates with exceptional accuracy.[14] Raman spectroscopy has further been explored as a culture-free approach to the evaluation of antibiotic susceptibility by monitoring spectral changes during the exposure of bacteria to selected antimicrobial agents.[12,15–21] Raman analysis has also shown significant potential for assessing antibiotic susceptibility without the need for drug exposure. For example, Raman spectroscopy can be used to directly identify transcriptomic features of antibiotic resistance,[12] and can differentiate susceptible vs. resistant strains with high confidence after model training using bacteria with different resistance profiles.[14]

These latter techniques make it possible to select an optimal treatment based on optical interrogation of a clinical sample without the need for cell culture or labeling reagents. However, due to the low scattering efficiency associated with Raman spectroscopy, high signal-to-noise ratios are necessary to extract sufficient signal for effective bacteria characterization. As a result, long data acquisition times and high bacteria concentrations are required, constraining the utility of conventional Raman detection for many clinical applications. To address this limitation, confocal Raman spectroscopy can significantly improve noise rejection and enable fingerprinting of small numbers of bacteria with short imaging times.[22] However, the femtoliter-scale detection volume associated with confocal optics imposes the need for highly time-consuming sample scanning to acquire target cells, making this approach unsuitable for high throughput diagnostics involving samples with low bacteria counts. A promising approach for overcoming the confocal Raman throughput constraint is to trap bacteria at a known location on a target substrate, allowing efficient spectra acquisition without the need for extensive sample scanning. To this end, a number of techniques for bacteria trapping have been explored. For example, optical tweezing has been widely used to capture individual bacteria for confocal detection,[23–29] and a variety of microfluidic-enabled trapping methods based on acoustic,[30] electrophoretic,[31] or dielectrophoretic[16,32–34] actuation have also been demonstrated for bacteria localization. A limitation for each of these techniques is that an active trapping mechanism is employed, adding cost and complexity, and potentially making these tools difficult to use in a clinical environment.

Here we describe a simple and fully passive bacteria trapping technique capable of capturing bacteria at a fixed location within a microfluidic chamber for confocal Raman analysis. As depicted in Fig. 1, the devices employ an angled nanogap structure for size-selective bacteria localization, with isolation and concentration of cells at the sharp tip of trap occurring by cell rolling during sample perfusion. A large nanogap perimeter allows sample to be delivered at high perfusion rates, with mobilization of cells by a rolling mechanism along the gap to reach the detection zone at the apex. Following bacteria trapping, the system is rinsed with fresh buffer to purify captured cells and reduce optical interference. In addition, the trap contents are dried without disrupting the bacteria focusing, eliminating background signal resulting from Raman scattering of water. The volume of the trapping zone is well matched to the confocal Raman optics, allowing high quality spectral data to be rapidly collected with minimal sample scanning. Because the microfluidic flow cell operates by passive perfusion of sample, rinse buffer, and air, it provides robust and reliable operation with minimal infrastructure. Here evaluate the performance of the nanogap technology for bacteria trapping and confocal Raman detection. A selection of both Gram positive and Gram negative pathogens are evaluated with an average of 100 cells used in each experiment. The resulting Raman measurements yield distinct spectral fingerprints that are found to match favorably with off-chip reference samples requiring manual scanning for spectrum acquisition.

Materials and Methods

Nanogap chip fabrication. The nanogap chip design consists of a 1 mm diameter and 20 μm deep circular chamber connected to 200 μm wide inlet and outlet channels patterned in a silicon wafer. The circular

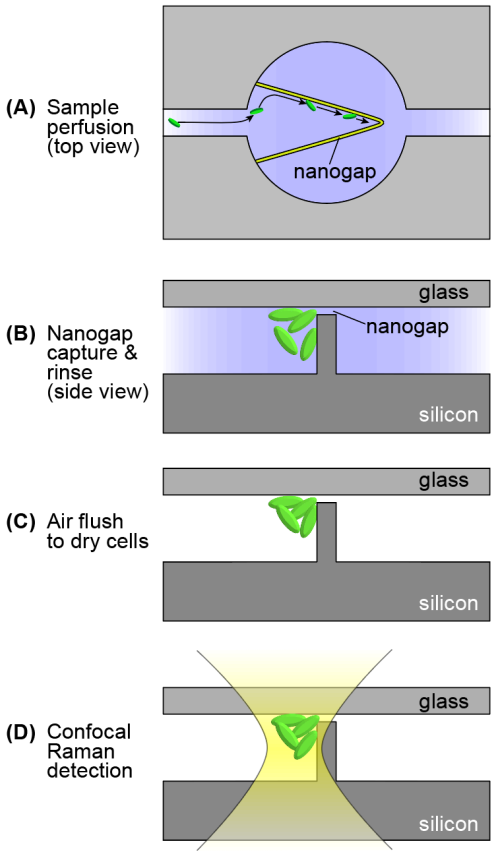

Figure 1: Nanogap-enabled bacteria trapping, concentration, and detection. (a) Sample fluid containing bacteria is perfused into an open chamber separated into two volumes by a 500 nm tall V-shaped gap. Rigid bacteria cells cannot enter the nanogap and accumulate along the gap entrance. (b) Buffer is perfused through the chip, forcing cells to roll along the trap entrance until reaching the tip. (c) The chip is rinsed and dried, and single-point confocal Raman detection is performed to extract spectral signatures from the trapped bacteria.

chamber is occluded by a V-shaped barrier selectively etched to a depth of 500 nm to form a nanogap between the top of the barrier and the upper sealing layer. The barrier possesses a 30° half-angle, and has a total length of 1645 µm. As depicted in Fig. 2A, the channel and nanogap structures were fabricated in a heavily-doped 100 mm diameter p-type Si wafer. The nanogap was first patterned by etching the circular chamber to a depth of 500 nm by reactive ion etching, followed by masking the barrier and etching the deeper regions of the chamber and the fluidic channels by silicon deep reactive ion etching (DRIE). The resulting nanogap was designed with a width of 10 µm. The wafer was diced into 2 cm square chips (Fig. 2B), and each chip was individually sealed using a 160 µm thick borosilicate glass coverslip (Borofloat 33, Schott, Jena, Germany) by anodic bonding. Before bonding, the coverslip was first patterned to form fluidic access ports using a dry film photoresist (RapidMask High-Tack, Ikonics Imaging, Duluth, MN) as a masking layer during abrasive glass etching using alumina microparticles by micro powder blasting (Accuflo MicroBlaster, Comco Inc., Burbank, CA). The patterned silicon and glass substrates were cleaned by piranha solution and manually aligned before sealing the channels via anodic bonding. Bonding was performed on a hot plate at 525 °C while applying a 500 V bias through a conductive pin pressed into the center of the glass/silicon stack with the silicon substrate held at 0 V. After bonding, fluid reservoirs

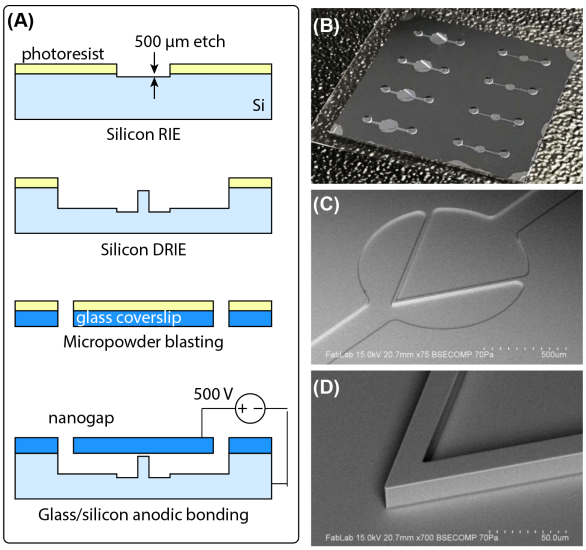

Figure 2: (A) Nanogap chip fabrication process comprising nanogap patterning, microchannel and focusing chamber patterning, port etching, and glass/silicon anodic bonding. (B) Fabricated glass/silicon chip with an array of devices with different trap chamber volumes. (C) SEM image of a single trap. (D) Magnified view of the trap apex where Raman detection is performed.

were formed by punching 2 mm diameter access ports in two pieces of fully cured polydimethylsiloxane (PDMS), and temporarily bonding the PDMS pieces to the glass cover plate with holes aligned to the inlet and outlet ports. Magnified images of the nanogap chamber and angled trap tip are provided in Fig. 2C and Fig. 2D, respectively.

Numerical modeling. The nanogap design was studied using the computational fluid dynamics (CFD) and particle tracing modules in COMSOL Multiphysics (COMSOL Inc., Burlington, MA). Simulation were performed through a two-step process. After first determining the steady-state fluid flow profile for time-independent laminar flow, the particle tracing module was applied to simulate time-dependent particle movements via bi-directionally coupled particle tracing within the laminar flow profile. Inlet flow velocity was set to 20 µm/s as the average linear velocity of a fully-developed flow. A no-slip boundary condition was applied to all surfaces except the inlet and outlet. The model geometry for the focusing chamber and nanogap structure was identical to the fabricated devices, but with analysis limited to a 250 µm axial chamber length to ensure numerical stability. For particle tracing, 2 µm diameter spherical particles were released at the model inlet. Size selection in the nanogap was approximated by assigning a conditional boundary at the nanogap entrance to diffusively scatter particles larger than 500 nm while preserving the kinetic energy of the particle. Wall lift forces were applied to all remaining boundaries and Stokes drag force was applied to all released particles.

Bacteria trapping. Before introducing bacteria solution into a nanogap chip, the device was first primed by pipetting 10 µL DI water directly into the PDMS outlet port, followed by withdraw of fluid through the inlet port using a manual syringe connected via Tygon tubing to a pipette tip inserted into the PDMS reservoir. The reversed flow used during priming served to minimize the potential for particulates to be introduced into the trap chamber. After verifying that no bubbles were trapped in the internal flow path by the priming solution, 100 µL of bacteria solution was added to the open inlet reservoir, and the pipette tip inserted into the outlet port was connected to a syringe pump operating in withdraw mode for sample perfusion. Experiments were performed using *Enterobacter cloacae*, *Klebsiella pneumoniae* and *Corynebacterium diphtheriae* as model pathogens. All three bacteria are rod-shaped with minor and major

axis dimensions of approximately 0.5 μm and 2 μm, respectively. To prepare bacteria samples, lyophilized powders of *C. cloacae*, *K. pneumoniae*, *C. diphtheriae* (Carolina Biological Supply, Burlington, NC) were separately cultured following the manufacturer's protocol in sterile glass tubes with Nutrient broth and tryptic soy broth (Carolina Biological Supply). Bacteria stock solutions were prepared by replacing the growth medium of the as-cultured bacteria with 1× phosphate buffered saline (PBS) via centrifugation to a concentration of 10^3 CFU/mL. For each solution, a 100 μL sample volume containing approximately 100 CFU was perfused through the nanogap device at 10 μL/min using a syringe pump for approximately 10 min until the entire sample was injected through the chip. After bacteria trapping, the device was rinsed with 30 μL 1× PBS followed by 100 μL DI water using the same process used for sample perfusion. Thorough DI rinsing was necessary to remove salts and other contaminants which can generate significant Raman background. Finally, ambient air was drawn through the device by applying weak vacuum to the outlet until all residual water is depleted, leaving a cluster of dried bacteria within the trap tip for Raman analysis. The time required to complete the entire sample introduction process including rinsing and air drying was approximately 30 min.

Reference sample preparation. Reference samples used for scanning confocal Raman imaging without nanogap processing were prepared by pipetting 20 μL of high concentration bacteria solution onto a clean glass slide, and allowing the slide to dry under a biosafety cabinet for 1 h at room temperature before confocal Raman imaging. The reference sample solutions were formed by replacing the growth medium of harvested bacteria with DI water to a final concentration of 10^7 CFU/mL. Dilutions were performed using DI water instead of PBS buffer to avoid Raman background signal associated with crystallized buffer salts in the dried sample spots.

Raman detection and peak analysis. Raman spectroscopy was performed using a Horiba LabRAM confocal Raman instrument equipped with a 50× NA 0.75 objective and 532 nm excitation laser. The selected lens provided a working distance of 330 μm, sufficient for imaging through the 160 μm thick glass chip lid. Following bacteria trapping, rinsing, and air drying, the nanogap chip was placed in the Raman microscope with the confocal detection volume positioned 3-4 μm behind the apex of the nanogap trap. Raman signal was acquired by averaging over 6 sequential measurements with a 10 s scan time per measurement. Following data collection, background estimation and correction was performed for each spectrum using the Statistics-sensitive Non-linear Iterative Peak-clipping (SNIP) algorithm implemented in the R programming language.[35,36] Automated peak identification from the spectroscopic data was performed using a deconvolution method integrated into the SNIP package.[37] Identical background estimation and peak identification parameters were employed for all samples including reference bacteria.

Results and Discussion

Devices were fabricated using 160 μm thick borosilicate glass coverslips to seal the microfluidic channels and form the upper surface of the nanogaps. In addition to supporting anodic bonding for reliable sealing to the silicon substrate, borosilicate glass was employed due to its relatively low background fluorescence during Raman analysis. The coverslip thickness was selected to support optical access to the trapping zone during confocal Raman imaging. One disadvantage to the low thickness is that the millimeter-scale trap chamber can act as a deformable membrane during sample perfusion, potentially altering the nanogap height and impacting the bacteria trapping process. For the 10 μL/min flow rate used in our studies, the approximate pressure across the glass layer was determined to be 0.16 atm based on plane Poiseuille flow through the gap, resulting in an estimated peak deflection of 120 nm based on an analytic model of deflection for a circular membrane.[38,39] Because the devices are operated by negative pressure, the estimated membrane deflection results in a moderate reduction in nanogap height, and is not expected to have a significant impact on the bacteria trapping process.

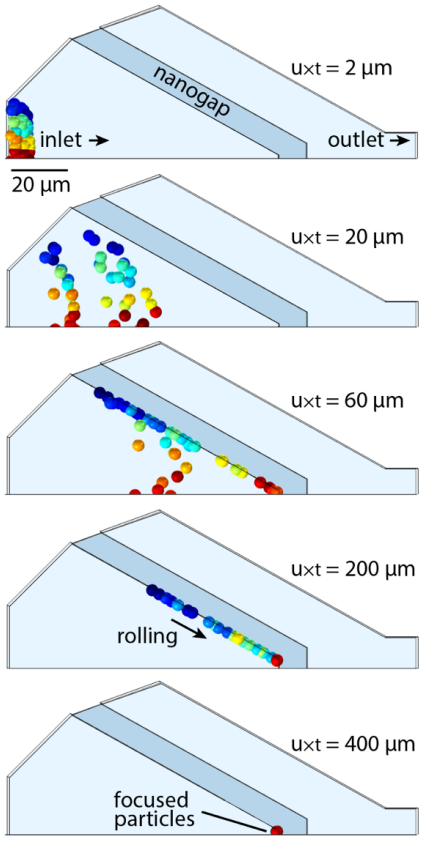

Figure 3: Simulation of bacteria trapping performed via COMSOL particle tracing. The inflow was set as fully developed flow and an average linear velocity of 20 µm/s was applied to ensure numerical stability. The characteristic transport length scale given by the product of mean flow velocity (u) and focusing time (t) is provided for each frame.

During sample perfusion within the nanogap devices, cells initially follow streamlines that traverse the nanogap, forcing bacteria to impact the gap barrier. The rigid cell structure limits bacteria deformation and limits intrusion of the cells into the gap, thereby accumulating bacteria at the gap opening while allowing smaller and more compliant contaminants such as cell lysis debris to pass through the gap unimpeded. This process is conceptually similar to prior work on compliance-based cell separation and concentration using an array of gap structures.[40] Because a component of the fluid momentum across the nanogap is aligned to the longitudinal axis of the chamber, bacterial cells are forced to roll along the gap opening toward the tip of the trap, and eventually accumulate at the apex. A numerical simulation depicting this process is presented in Fig. 3. In this model, rigid spherical particles released upstream of the chamber tip advect to the nanogap opening under the influence of bulk fluid flow. Upon reaching the gap, particles are prevented from following the streamlines through the gap by size exclusion within the sub-micrometer opening. The constrained particles roll along the gap wall towards the chamber tip due to the presence of a flow velocity component parallel to the wall. The average particle velocity along the trap wall remains constant during this process with a value approximately 20% of the bulk flow velocity through the nanogap itself. As expected, particles migrate to the tip of the chamber where they are immobilized.

We note that this simple rigid sphere model provides an idealized view of the bacteria trapping process that ignores interactions between the bacteria and nanogap wall that can impact both the transport rate and

fate of bacteria during perfusion. In particular, several factors that may impede transport are not considered. For example, adhesive wall interactions are not included in the model, nor are forces associated with flow near the nanogap wall, where bounded shear flow can reduce transport parallel to the wall surface.[41,42] At the same time, several interactions that serve to counteract these retarding factors are also not considered, including wall-induced lift forces and repulsive electrostatic interactions between the negative charges associated with the SiO_2 channel surfaces and bacterial lipoproteins[43–45]. A more significant factor impacting bacteria transport is elastic deformation of the due cells to viscous drag force normal to the nanogap wall. The plasma membrane of both Gram-positive and Gram-negative bacteria is encased by a rigid peptidoglycan layer that confers high stiffness, allowing bacterial cells to withstand at least several atmospheres of intracellular pressure without rupture.[46,47] While the elastic moduli of many bacteria can be in the range of 50-200 MPa,[47] small cell deformations during perfusion may still lead to cell immobilization within the nanogaps. For a rod-shaped bacterium in viscous shear flow, shear stresses arising from the velocity gradient of the flow field will induce the cell to align its major axis to the local streamlines.[48,49] Because the minor axis dimensions of the bacteria used in this study are similar to the designed gap height, penetration of flow-aligned bacteria into the gap can occur at relatively low forces. This behavior was evaluated as a function of flow rate within the nanogap chips. While higher perfusion rates were observed to result in increased bacteria loss within the nanogaps. limiting the maximum flow rate to 10 µL/min was found to ensure cell loss below 5% for the specific device dimensions studied here.

Bacteria trapping and confocal Raman analysis experiments were performed using pathogenic *E. cloacae*, *K. pneumoniae*, and *C. diphtheriae* bacteria. Multi-drug resistant strains of each pathogen have emerged in recent years that present an increased challenge for clinical treatment.[50–52] *E. cloacae* is a Gram-negative bacterium that is a routine cause of infection in healthcare settings.[53] *K. pneumoniae* is a Gram-negative bacterium that is also associated with multiple nosocomial infections, including pneumonia, meningitis, wound infections, and bloodstream infections.[54] *C. diphtheriae* is a Gram-positive, pathogenic bacterium that causes diphtheria.[55] Following the perfusion and trapping of approximately 100 CFU of each bacterium through a nanogap device, single-point confocal Raman spectroscopy was performed at the defined trapping point. Detection was performed with the Raman microscope focus positioned axially along the centerline of the perfusion chamber and approximately 3-4 µm in front of the chamber apex (Fig. 4A), and vertically 3-4 µm below the bottom surface of the glass lid. This position was selected to maximum bacteria signal while avoiding interference from the silicon substrate. The Raman background of the silicon surface was also measured from the tip of the nanogap trap, as shown in Fig. 4B.

The resulting Raman spectra collected after trapping each bacteria sample are presented in Fig. 5. Reference spectra obtained using high concentration cell suspensions deposited onto bare glass cover slips are also provided in this figure. The reference spectra were collected by manual scanning of the deposited cells performed to maximize signal, providing a direct comparison to conventional Raman analysis of high concentration bacteria samples. The SNIP algorithm[35,36] was used to subtract the silicon background

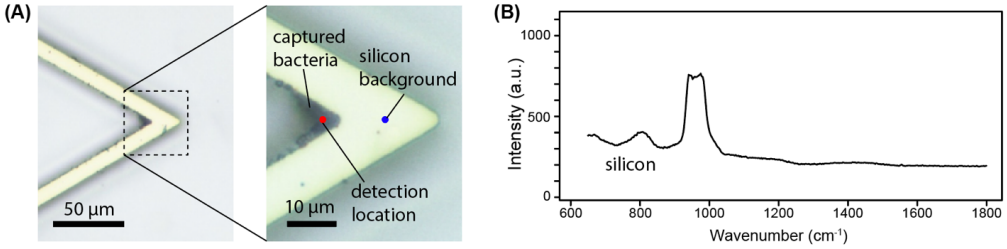

Figure 4: (A) Optical micrograph showing trapped E. cloacae bacteria at the nanogap tip. Raman detection was performed at a point 3-4 µm behind the tip to reduce background signal from the silicon surface. (B) Typical background spectrum collected from the silicon trap surface and used during background subtraction in subsequent bacteria analyses.

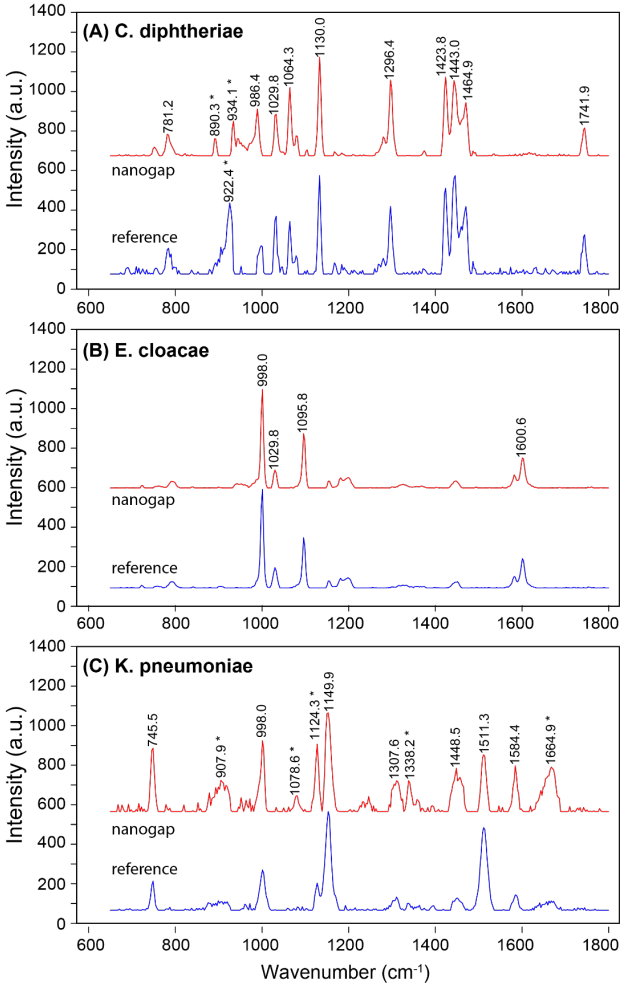

Figure 5: Raman spectra acquired following capture of (A) *C. diphtheriae*, (B) *E. cloacae*, and (C) *K. pneumoniae* bacteria in a nanogap chip. Matching spectra for samples deposited on a bare cover slip are shown for each bacterium. Peaks identified in either the nanogap or reference spectrum but absent from the corresponding spectrum are denoted with an asterisk (*).

signal, and automated peak identification was performed through deconvolution of the processed spectra.[37] As can be seen in Fig. 5, there is excellent agreement between individual peaks within the on-chip and reference spectra for each organism. With the exception of a single reference peak for *C. diphtheriae* that is not found in the corresponding nanogap spectrum, all peaks detected from the reference samples are also identified from the measurements performed using the nanogap chip. Significantly, on-chip Raman analysis of the focused bacteria resulted in the identification of 2 peaks for *C. diphtheriae* and 5 peaks for *K. pneumoniae* that were not observed from the high concentration reference samples.

The minimum number of perfused cells required for effective detection in the nanogap chips is a function of bacteria trapping efficiency, which is largely dependent on cell loss during the concentration process. The performance enhancement observed for the nanogap measurements is believed to result from dense packing of immobilized cells within the Raman detection volume. Initial cell concentrations in these experiments were selected to perfuse a total of approximately 100 bacteria cells through the nanogap chips. While dense cell clusters were successfully generated at the trap tips, significant numbers of cells were often lost during perfusion, with as few as 20-30% of the injected cells typically found to be

concentrated at the trap apex under the selected sample loading conditions. The dominant mechanism for cell loss was mechanical confinement of cells along the length of the nanogap upstream of the chamber tip, with some bacteria found anchored at the inner surface of the gap and other cells partially or fully inserted into the gap itself. As a result, efforts to characterize samples with lower bacteria counts resulted in irreproducible Raman spectra. To reduce the limit of detection for the nanogap technology, further studies are needed improve capture efficiency through optimization of the nanogap dimensions, for example by reducing the gap width to lower the pressure gradient required for sample perfusion. Within the current detection limit of approximately 100 cells, the nanogap chips offer an attractive path toward rapid bacteria identification from microliter-scale sample volumes for a wide range of clinical applications where high bacteria concentrations are common. For example, in the case of intra-abdominal infections, clinically-relevant bacteria concentrations are greater than 10^8 CFU/mL in both pus and peritoneal fluids,[56] while bile duct infection is defined by colonization levels above 10^4 CFU/mL.[57] Similarly, urinary tract infections routinely exhibit bacteria concentrations above 10^4 CFU/mL.[58] However, improved capture efficiency will be required for applications involving significantly lower bacteria concentrations, such as bloodstream infections where detecting pathogens in the range of 1-10 CFU/mL is required.[59]

Conclusion

The nanogap devices enable rapid and effective isolation and concentration of bacteria from dilute suspensions of both Gram positive and Gram negative pathogens. By concentrating bacteria into a confined region at the trap tip that is well matched to the femtoliter-scale detection volume for the confocal optics of the Raman system, high signal-to-background ratios in the resulting Raman spectra were achieved from a 100 μL sample volume, with a detection limit of approximately 100 cells in the initial sample. Single-point detection in the nanogap chips enabled the acquisition of spectral signatures for each pathogen with signature content exceeding that acquired from high-concentration reference samples where manual scanning is required to optimize Raman signal. We believe that the speed, simplicity, and automation of the passive flow-through technology make the nanogap Raman chips attractive for a wide range of clinical applications.

Acknowledgements

This work was supported by the National Institutes of Health through grant R01AI15356401. The authors acknowledge the support of the University of Maryland Nanocenter FabLab for device fabrication and the Surface Analysis Center for device characterization.

Data Availability

The data that support the findings of this study are available from the corresponding author upon reasonable request.

References

[1] *Antibiotic Resistance Threats in the United States* (CDC Report, 2019).
[2] L. Váradi, J.L. Luo, D.E. Hibbs, J.D. Perry, R.J. Anderson, S. Orenga, and P.W. Groundwater, **46**, 4818 (2017).
[3] F.P. Maurer, M. Christner, M. Hentschke, and H. Rohde, Infect. Dis. Rep. (2017).
[4] B.A. Lipsky, M. Dryden, F. Gottrup, D. Nathwani, R.A. Seaton, and J. Stryja, J. Antimicrob. Chemother. **71**, 3026 (2016).
[5] E. Avdic and K.C. Carroll, Infect. Dis. Clin. North Am. (2014).
[6] R. Franco-Duarte, L. Černáková, S. Kadam, K.S. Kaushik, B. Salehi, A. Bevilacqua, M.R. Corbo, H.

315 Antolak, K. Dybka-Stępień, M. Leszczewicz, S. Relison Tintino, V.C. Alexandrino de Souza, J. Sharifi-
316 Rad, H.D.M. Coutinho, N. Martins, and C.F. Rodrigues, Microorganisms **7**, (2019).
317 [7] R.R. Jones, D.C. Hooper, L. Zhang, D. Wolverson, and V.K. Valev, Nanoscale Res. Lett. **14**, 231
318 (2019).
319 [8] W.R. Premasiri, J.C. Lee, A. Sauer-Budge, R. Théberge, C.E. Costello, and L.D. Ziegler, Anal.
320 Bioanal. Chem. **408**, 4631 (2016).
321 [9] S. Pahlow, S. Meisel, D. Cialla-May, K. Weber, P. Rösch, and J. Popp, Adv. Drug Deliv. Rev. (2015).
322 [10] S. Stöckel, J. Kirchhoff, U. Neugebauer, P. Rösch, and J. Popp, J. Raman Spectrosc. **47**, 89 (2016).
323 [11] B. Lorenz, C. Wichmann, S. Stöckel, P. Rösch, and J. Popp, Trends Microbiol. **25**, 413 (2017).
324 [12] A. Germond, T. Ichimura, T. Horinouchi, H. Fujita, C. Furusawa, and T.M. Watanabe, Commun.
325 Biol. **1**, 85 (2018).
326 [13] K.C. Henderson, A.J. Benitez, A.E. Ratliff, D.M. Crabb, E.S. Sheppard, J.M. Winchell, R.A. Dluhy,
327 K.B. Waites, T.P. Atkinson, and D.C. Krause, PLoS One **10**, e0131831 (2015).
328 [14] C.-S. Ho, N. Jean, C.A. Hogan, L. Blackmon, S.S. Jeffrey, M. Holodniy, N. Banaei, A.A.E. Saleh, S.
329 Ermon, and J. Dionne, Nat. Commun. **10**, 4927 (2019).
330 [15] U. Münchberg, P. Rösch, M. Bauer, and J. Popp, Anal. Bioanal. Chem. **406**, 3041 (2014).
331 [16] U.C. Schröder, C. Beleites, C. Assmann, U. Glaser, U. Hübner, W. Pfister, W. Fritzsche, J. Popp, and
332 U. Neugebauer, Sci. Rep. **5**, 8217 (2015).
333 [17] L. Teng, X. Wang, X. Wang, H. Gou, L. Ren, T. Wang, Y. Wang, Y. Ji, W.E. Huang, and J. Xu, Sci.
334 Rep. **6**, 34359 (2016).
335 [18] U.C. Schröder, J. Kirchhoff, U. Hübner, G. Mayer, U. Glaser, T. Henkel, W. Pfister, W. Fritzsche, J.
336 Popp, and U. Neugebauer, J. Biophotonics **10**, 1547 (2017).
337 [19] Y. Tao, Y. Wang, S. Huang, P. Zhu, W.E. Huang, J. Ling, and J. Xu, Anal. Chem. **89**, 4108 (2017).
338 [20] C. Assmann, J. Kirchhoff, C. Beleites, J. Hey, S. Kostudis, W. Pfister, P. Schlattmann, J. Popp, and U.
339 Neugebauer, Anal. Bioanal. Chem. **407**, 8343 (2015).
340 [21] A.I.M. Athamneh, R.A. Alajlouni, R.S. Wallace, M.N. Seleem, and R.S. Senger, Antimicrob. Agents
341 Chemother. **58**, 1302 (2014).
342 [22] D. Wang, P. He, Z. Wang, G. Li, N. Majed, and A.Z. Gu, Curr. Opin. Biotechnol. **64**, 218 (2020).
343 [23] C. Xie, J. Mace, M.A. Dinno, Y.Q. Li, W. Tang, R.J. Newton, and P.J. Gemperline, Anal. Chem. **77**,
344 4390 (2005).
345 [24] D. V Petrov, J. Opt. A Pure Appl. Opt. **9**, S139 (2007).
346 [25] C. Xie, C. Goodman, M.A. Dinno, and Y.-Q. Li, Opt. Express **12**, 6208 (2004).
347 [26] J.W. Chan, A.P. Esposito, C.E. Talley, C.W. Hollars, S.M. Lane, and T. Huser, Anal. Chem. **76**, 599
348 (2004).
349 [27] C. Xie and Y. Li, J. Appl. Phys. **93**, 2982 (2003).
350 [28] T. Dahlberg, D. Malyshev, P.O. Andersson, and M. Andersson, in *Chem. Biol. Radiol. Nucl. Explos.*
351 *Sens. XXI*, edited by J.A. Guicheteau and C.R. Howle (SPIE, 2020), p. 28.
352 [29] F. Sinjab, D. Awuah, G. Gibson, M. Padgett, A.M. Ghaemmaghami, and I. Notingher, Opt. Express
353 **26**, 25211 (2018).
354 [30] V.O. Baron, M. Chen, B. Hammarstrom, R.J.H. Hammond, P. Glynne-Jones, S.H. Gillespie, and K.
355 Dholakia, Commun. Biol. **3**, 236 (2020).
356 [31] B. Krafft, A. Tycova, R.D. Urban, C. Dusny, and D. Belder, Electrophoresis **42**, 86 (2021).
357 [32] H.-Y. Lin, C.-H. Huang, W.-H. Hsieh, L.-H. Liu, Y.-C. Lin, C.-C. Chu, S.-T. Wang, I.-T. Kuo, L.-K.
358 Chau, and C.-Y. Yang, Small **10**, 4700 (2014).
359 [33] I.-F. I-Fang Cheng, H.-C. Chang, T.-Y. Chen, C. Hu, and F.-L. Yang, Sci. Rep. **3**, 2365 (2013).
360 [34] X. Chen, Z. Liang, D. Li, Y. Xiong, P. Xiong, Y. Guan, S. Hou, Y. Hu, S. Chen, G. Liu, and Y. Tian,
361 Biosens. Bioelectron. **99**, 416 (2018).
362 [35] C.G. Ryan, E. Clayton, W.L. Griffin, S.H. Sie, and D.R. Cousens, Nucl. Instruments Methods Phys.
363 Res. Sect. B Beam Interact. with Mater. Atoms **34**, 396 (1988).
364 [36] M. Morháč and V. Matoušek, Appl. Spectrosc. **62**, 91 (2008).

[37] M. Morháč, J. Kliman, V. Matoušek, M. Veselský, and I. Turzo, Nucl. Instruments Methods Phys. Res. Sect. A Accel. Spectrometers, Detect. Assoc. Equip. **443**, 108 (2000).
[38] S. Timoshenko and S. Woinoskly-Krieger, *Theory of Plates and Shells* (McGraw-Hill, 1959).
[39] F. Bitsie, W.P. Eaton, D.W. Plummer, and J.H. Smith, in *Proc. Int. Conf. Model. Simul. Microsystems* (San Juan, Puerto Rico, 1999), pp. 640–643.
[40] G. Wang, W. Mao, R. Byler, K. Patel, C. Henegar, A. Alexeev, and T. Sulchek, PLoS One **8**, e75901 (2013).
[41] C. Jayageeth, V.I. Sharma, and A. Singh, Int. J. Multiph. Flow **35**, 261 (2009).
[42] E. Gavze and M. Shapiro, Int. J. Multiph. Flow **23**, 155 (1997).
[43] A.M. Elmahdy, S.E. El-Mofty, N.A. Abdel-Khalek, and A.A. El-Midany, Adsorpt. Sci. Technol. **29**, 47 (2011).
[44] X. Hua, Z. Wu, H. Zhang, D. Lu, M. Wang, Y. Liu, and Z. Liu, Chemosphere **80**, 951 (2010).
[45] T. Velkov, Z.Z. Deris, J.X. Huang, M.A.K. Azad, M. Butler, S. Sivanesan, L.M. Kaminskas, Y.-D. Dong, B. Boyd, M.A. Baker, M.A. Cooper, R.L. Nation, and J. Li, Innate Immun. **20**, 350 (2014).
[46] J. V Höltje, Microbiol. Mol. Biol. Rev. **62**, 181 (1998).
[47] H.H. Tuson, G.K. Auer, L.D. Renner, M. Hasebe, C. Tropini, M. Salick, W.C. Crone, A. Gopinathan, K.C. Huang, and D.B. Weibel, Mol. Microbiol. **84**, 874 (2012).
[48] R. Rusconi, J.S. Guasto, and R. Stocker, Nat. Phys. **10**, 212 (2014).
[49]Proc. R. Soc. London. Ser. A, Contain. Pap. a Math. Phys. Character **102**, 161 (1922).
[50] M.K. Annavajhala, A. Gomez-Simmonds, and A.-C. Uhlemann, Front. Microbiol. **10**, 44 (2019).
[51] M. Bassetti, E. Righi, A. Carnelutti, E. Graziano, and A. Russo, Expert Rev. Anti. Infect. Ther. **16**, 749 (2018).
[52] T.M. Walker, M. Merker, A.M. Knoblauch, P. Helbling, O.D. Schoch, M.J. van der Werf, K. Kranzer, L. Fiebig, S. Kröger, W. Haas, H. Hoffmann, A. Indra, A. Egli, D.M. Cirillo, J. Robert, T.R. Rogers, R. Groenheit, A.T. Mengshoel, V. Mathys, M. Haanperä, D. van Soolingen, S. Niemann, E.C. Böttger, P.M. Keller, and MDR-TB Cluster Consortium, Lancet. Infect. Dis. **18**, 431 (2018).
[53] R. Keller, M.Z. Pedroso, R. Ritchmann, and R.M. Silva, Infect. Immun. **66**, 645 (1998).
[54] Y. Keynan and E. Rubinstein, Int. J. Antimicrob. Agents **30**, 385 (2007).
[55] P.A. Hoskisson, Microbiology **164**, 865 (2018).
[56] C. Konig, H.-P. Simmen, and J. Blaser, J. Antimicrob. Chemother. **42**, 227 (1998).
[57] M. Kaya, R. Beştaş, F. Bacalan, F. Bacaksız, E.G. Arslan, and M.A. Kaplan, World J. Gastroenterol. **18**, 3585 (2012).
[58] M.S. Najar, C.L. Saldanha, and K.A. Banday, Indian J. Nephrol. **19**, 129 (2009).
[59] O. Opota, A. Croxatto, G. Prod'hom, and G. Greub, Clin. Microbiol. Infect. **21**, 313 (2015).